Interface dynamics, instabilities, and solute bands in rapid directional solidification

M. Conti
Dipartimento di Matematica e Fisica, Universita' di Camerino and Istituto Nazionale di Fisica della Materia, 62032 Camerino, Italy
(Received 20 January 1998)

In rapid solidification experiments on metallic alloys structures have been observed which are periodic along the growth direction. The origin of these *banded structures* has been ascribed to an oscillatory instability of the solid-liquid interface characterized by large variations of the interface velocity; this instability was predicted by several authors incorporating nonequilibrium effects into the classic Mullins-Sekerka analysis. In this paper the rapid solidification of a binary alloy, directed by a moving temperature field, is studied with the phase-field model; in a region of the parameter space an oscillatory instability is evidenced, which reflects in alternating low and high concentration solute bands. The equations of the model are numerically solved to show under what conditions (i.e., isotherm velocity and temperature gradient) the banded structure can be observed. In many respects the results agree with the linear stability analysis of the free-boundary equations performed by Merchant and Davis [G. J. Merchant and S. H. Davis, Acta Metall. Mater. **38**, 2683 (1990)]; we detected also significant deviations which trace their roots to the diffuse solid-liquid interface characteristic of the phase-field model, opposed to the zero dimension interface of the free-boundary model. [S1063-651X(98)08807-2]

PACS number(s): 81.10.Aj, 05.70.Ln, 64.70.Dv

I. INTRODUCTION

In rapid solidification experiments on various binary alloys, at growth rates close to the absolute stability limit structures have been observed which are periodic along the growth direction [1–4]. These structures consist of a regular succession of dark and light bands, parallel to the solid-liquid front, with a band spacing ranging from 0.3 to 1.5 μm. The dark bands have a precipitate structure, either cellular dendritic or eutectic, depending on the alloy composition; the light bands are formed of precipitation-free solid solution, with a composition that is uniform and equal to the nominal concentration of the alloy. It has been argued [5] that planar front growth in absolute stability is responsible for the formation of the light bands.

At first, the physical origin of the banded structure was not clearly understood, as it was not expected within the classic Mullins-Sekerka analysis [6]; however, very soon it was realized that departures from local interface equilibrium, neglected in this former approach, could result in a richer behavior of the dynamics of the moving interface.

Coriell and Sekerka [7] modified the linear stability analysis to account for nonequilibrium effects via a velocity dependent segregation coefficient $k(v)$, defined as the ratio c_s/c_l of the solute concentration in the growing solid to that in the liquid at the interface. Along the same lines Merchant and Davis [8] incorporated into the problem the results of the continuous growth model of Aziz [9] and Aziz and Kaplan [10], allowing the segregation coefficient k and the interface temperature T_I to depend on the interface velocity v in a thermodynamically consistent way. These studies led to identification of an oscillatory instability characterized by an infinite wavelength along the solid-liquid front; this instability should be related to the mechanism of band formation.

The above studies assumed an infinite thermal diffusivity, resulting in a uniform temperature gradient along the growth direction. Subsequently Huntley and Davis [11] and Karma and Sarkissian [12,13] relaxed this hypothesis, accounting for the diffusion of the latent heat released at the interface. The most relevant consequence of this effect is the reduction of the parameter range where the banded structure should occur; moreover a restabilization effect at zero wave number was also detected. It was also shown, in a numerical study conducted with the Greens-function technique [13], that the oscillatory instability actually leads, in a nonlinear regime, to time-periodic changes in interface velocity and interface temperature, which reflect in periodic variations of the solute concentration along the growth direction (the so-called *solute bands*).

To better understand the mechanism underlying the formation of the banded structure, a different approach could be based on the phase-field model (PFM). Within this method a phase field $\phi(x,t)$ characterizes the phase of the system at each point. A free-energy (or entropy) functional is then constructed, that depends on ϕ as well as on the temperature and concentration fields T,c; a $(\nabla\phi)^2$ term accounts for the energy cost associated to the solid-liquid interface. The extremization of the functional with respect to these variables results in the dynamic equations for the evolution of the process. This approach was pioneered by Caginalp and Fife in a series of studies [14–16] and was initially applied to the solidification of pure substances [17–21]; subsequently the PFM was extended to describe the solidification of binary alloys [22–28]. Several studies both analytical [16–18] and numerical [19–21] established on a firm basis the notion that the phase-field model for a pure substance, in the limit of a vanishingly small interface width, reduces to the sharp interface diffusional equations, incorporating in a natural fashion the Gibbs-Thomson effect as well as the kinetic undercooling of the moving interface. Moreover, the PFM for binary alloys, in the formulation given below, accounts for nonequilibrium effects as solute trapping, recovering the results predicted by the continuous growth model for steady growth conditions [27].

In the present study the rapid solidification of a binary alloy, driven by a moving temperature field, is simulated in

one dimension through the phase-field model. Due to numerical tractability, the effect of the latent heat diffusion is neglected; nevertheless we hope to capture the most relevant characteristics of the process. It will be shown that an oscillatory instability arises in a region of the parameter space where the driving force for solidification (the dynamic undercooling) is a decreasing function of the associated flux (the growth rate). When the operating point of the process is selected in this region, the interface velocity and temperature undergo large oscillations originating low and high concentration solute bands.

The picture of the process given by the present study agrees in many respects with the free-boundary formulation of the problem, integrated with the constitutional laws $T_I(v)$ and $k(v)$ resulting from the continuous growth model; however, we detected also significant deviations, which trace their roots to the diffuse solid-liquid interface intrinsic to the phase-field model, opposed to the zero-dimension interface of the free-boundary equations.

The paper is organized as follows. In Sec. II the governing equations of the model will be derived, through the extremization of an entropy functional. In Sec. III some details of the numerical method will be given, and in Sec. IV the results of the numerical simulations will be presented and discussed. The conclusions will follow in Sec. V. A brief summary of the present work has recently been published in a Rapid Communication [29].

II. DESCRIPTION OF THE MODEL

A. Derivation of the governing equations

The model describes the directional solidification of an ideal solution of components A (solvent) and B (solute), in terms of three fields: the scalar phase field ϕ, the local solute concentration c, and the temperature T. The field ϕ is an order parameter assuming the values $\phi=0$ in the solid and $\phi=1$ in the liquid; intermediate values correspond to the interface between the two phases. As a starting point an entropy functional is defined as

$$\mathcal{S}=\int\left[s(e,\phi,c)-\frac{\epsilon^2}{2}\,|\nabla\phi|^2\right]dv, \tag{1}$$

where integration is performed over the system volume; the last term in the integrand is a gradient correction to the thermodynamic entropy density s, that depends on the internal energy density e and on the concentration and phase fields through the thermodynamic relations:

$$\frac{\partial s}{\partial e}=\frac{1}{T}, \tag{2}$$

$$\frac{\partial s}{\partial c}=\frac{\mu^A-\mu^B}{T}, \tag{3}$$

$$\frac{\partial s}{\partial \phi}=-\frac{1}{T}\frac{\partial}{\partial \phi}\left[(1-c)\mu^A+c\mu^B\right]. \tag{4}$$

In Eqs. (3) and (4) μ^A and μ^B are the chemical potentials of the solvent and the solute, given for an ideal solution, respectively, by

$$\mu^A=f^A(\phi,T)+\frac{RT}{v_m}\ln(1-c), \tag{5}$$

$$\mu^B=f^B(\phi,T)+\frac{RT}{v_m}\ln(c). \tag{6}$$

Here R is the gas constant and v_m is the molar volume; f^A is the free energy density of the pure species A, taken in the form

$$f^A=TG^A(\phi)+p(\phi)L^A\left(1-\frac{T}{T^A}\right)-CT\,\ln\left(\frac{T}{T^A}\right), \tag{7}$$

with L^A and T^A representing the latent heat per unit volume and the melting temperature of pure A; C is the specific heat, for which we assume constant and equal values for both phases and materials. In Eq. (7) the function $G^A(\phi)$ is given by

$$G^A(\phi)=\frac{1}{4}\,\tilde{W}^A\phi^2(1-\phi)^2=\tilde{W}^A g(\phi) \tag{8}$$

that is a symmetric double well potential with equal minima at $\phi=0$ and 1, scaled by the positive well height $\tilde{W}^A$.

Choosing the function $p(\phi)$ as $p(\phi)=\phi^3(10-15\phi+6\phi^2)$ the condition is enforced that bulk solid and liquid are described by $\phi=0$ and 1, respectively, for every value of temperature [18].

Equation (7) still holds for the free energy f^B if all the material parameters labeled with the superscript A, are replaced with the ones related to the B species.

A conservation law governs the solute transport:

$$\dot{c}=-\nabla\cdot\mathbf{J}_c\,. \tag{9}$$

To ensure that the local entropy production is always positive, the solute flux can be written in a simple form as

$$\mathbf{J}_c=M_c\nabla\,\frac{\delta\mathcal{S}}{\delta c} \tag{10}$$

and the evolution of the phase field is given by

$$\dot{\phi}=M_\phi\,\frac{\delta\mathcal{S}}{\delta\phi}, \tag{11}$$

where M_c and M_ϕ are positive constants.

Evaluating the variational derivatives gives the dynamic equation for the phase field in the form

$$\frac{\partial\phi}{\partial t}=M_\phi[\epsilon^2\nabla^2\phi-(1-c)\tilde{H}^A(\phi,T)-c\tilde{H}^B(\phi,T)], \tag{12}$$

where the function $\tilde{H}^A(\phi,T)$ is defined as

$$\tilde{H}^A(\phi,T)=G'(\phi)-p'(\phi)L^A\,\frac{T-T^A}{TT^A} \tag{13}$$

and a similar expression holds for $\tilde{H}^B(\phi,T)$.

Starting from Eqs. (3), (9), and (10) and observing that

$$\nabla\frac{\mu^A-\mu^B}{T}=\frac{\partial}{\partial\phi}\frac{\mu^A-\mu^B}{T}\nabla\phi+\frac{\partial}{\partial c}\frac{\mu^A-\mu^B}{T}\nabla c+\frac{\partial}{\partial T}\frac{\mu^A-\mu^B}{T}\nabla T, \tag{14}$$

where

$$\frac{\partial}{\partial\phi}\frac{\mu^A-\mu^B}{T}=\tilde{H}^A(\phi,T)-\tilde{H}^B(\phi,T), \tag{15}$$

$$\frac{\partial}{\partial c}\frac{\mu^A-\mu^B}{T}=-\frac{R}{v_m}\frac{1}{c(1-c)}, \tag{16}$$

$$\frac{\partial}{\partial T}\frac{\mu^A-\mu^B}{T}=\tilde{\Gamma}(\phi,T), \tag{17}$$

with the function $\tilde{\Gamma}(\phi,T)$ defined as

$$\tilde{\Gamma}(\phi,T)=-\frac{p(\phi)}{T^2}(L^A-L^B) \tag{18}$$

the dynamic equation for the concentration field is written as

$$\frac{\partial c}{\partial t}=-\nabla\cdot\left\{D_c c(1-c)\frac{v_m}{R}[\tilde{H}^A(\phi,T)-\tilde{H}^B(\phi,T)]\nabla\phi-D_c\nabla_c+D_c c(1-c)\frac{v_m}{R}\tilde{\Gamma}(\phi,T)\nabla T\right\}. \tag{19}$$

In Eq. (19) the standard definition of the solute diffusivity D_c has been recovered taking

$$D_c=\frac{M_c}{c(1-c)}\frac{R}{v_m}. \tag{20}$$

To allow for different diffusivities in the solid and liquid phases, in the following D_c will be taken as

$$D_c=D_s+p(\phi)(D_l-D_s), \tag{21}$$

D_l and D_s being the diffusivities in the liquid and in the solid, respectively.

As we neglect the latent heat diffusion, the temperature field is decoupled from the phase and concentration fields, and is represented as a traveling wave moving towards the positive x direction with uniform gradient $\tilde{G}$ and constant velocity $\tilde{V}_0$:

$$\frac{\partial T}{\partial t}=-\tilde{V}_0\frac{\partial T}{\partial x}=-\tilde{V}_0\tilde{G}. \tag{22}$$

The model is then synthesized through Eqs. (12), (19), and (22).

B. The nondimensional equations and the model parameters

The problem will be treated scaling lengths to some reference length ξ and time to ξ^2/D_l. Allowing M_ϕ to depend on the local composition as

$$M_\phi=(1-c)M_\phi^A+cM_\phi^B \tag{23}$$

and following the lines suggested by Warren and Boettinger [28] to associate the model parameters to the material properties, the governing equations become

$$\frac{\partial\phi}{\partial t}=[(1-c)m^A+cm^B][\nabla^2\phi+(1-c)Q^A(T,\phi)+cQ^B(T,\phi)], \tag{24}$$

$$\frac{\partial c}{\partial t}=\nabla\cdot\{\lambda(\phi)\nabla c-c(1-c)\lambda(\phi)[H^A(\phi,T)-H^B(\phi,T)]\times\nabla\phi-c(1-c)\lambda(\phi)\Gamma(\phi,T)\nabla T\}, \tag{25}$$

$$\frac{\partial T}{\partial t}=-V_0\frac{\partial T}{\partial x}=-V_0G, \tag{26}$$

where

$$H^{A,B}(\phi,T)=W^{A,B}\frac{dg(\phi)}{d\phi}-L^{A,B}\frac{v_m}{R}\frac{dp(\phi)}{d\phi}\frac{T-T^{A,B}}{TT^{A,B}}=\frac{v_m}{R}\tilde{H}^{A,B}(\phi,T), \tag{27}$$

$$Q^{A,B}(\phi,T)=-\frac{\xi^2}{(h^{A,B})^2}\frac{dg(\phi)}{d\phi}+\frac{1}{6\sqrt{2}}\frac{\xi^2L^{A,B}}{\sigma^{A,B}h^{A,B}}\frac{T-T^{A,B}}{T_I}\frac{dp(\phi)}{d\phi}, \tag{28}$$

$$\Gamma(\phi,T)=\frac{v_m}{R}\tilde{\Gamma}(\phi,T), \tag{29}$$

$$\lambda(\phi)=\frac{D_s}{D_l}+p(\phi)\left(1-\frac{D_s}{D_l}\right), \tag{30}$$

$$V_0=\tilde{V}_0\frac{\xi}{D_l},\quad G=\tilde{G}\xi. \tag{31}$$

In Eq. (28) $\sigma^{A,B}$, $h^{A,B}$ indicate the surface tension and the interface thickness of the pure components A and B, respectively; T_I is the initial (equilibrium) interface temperature. The model parameters $m^{A,B}$, $W^{A,B}$ depend on the physical properties of the alloy components through

$$m^{A,B}=\frac{\beta^{A,B}\sigma^{A,B}T^{A,B}}{D_lL^{A,B}},\quad W^{A,B}=\frac{12}{\sqrt{2}}\frac{v_m}{R}\frac{\sigma^{A,B}}{T^{A,B}h^{A,B}}, \tag{32}$$

where $\beta^{A,B}$ is the kinetic undercooling coefficient of pure A or B, that relates the interface undercooling to the interface velocity v through $v=\beta^{A,B}(T^{A,B}-T_I)$. Notice that Eqs. (32) were derived using the equilibrium planar solution of the phase-field equations, which gives $h^{A,B}=\epsilon\sqrt{\tilde{W}^{A,B}}$; $\sigma^{A,B}=(\epsilon T^{A,B}/\sqrt{\tilde{W}^{A,B}})/(6\sqrt{2})$ [28].

To estimate the above parameters we referred to the thermophysical properties of nickel (solvent) and copper (solute), summarized in Table I. The length scale was fixed at $\xi=2.1\times10^{-4}$ cm; the kinetic undercooling coefficients were

TABLE I. Material parameters for the Ni-Cu alloy.

	Nickel	Copper
T_m (K)	1728	1358
L (J/cm^3)	2350	1728
v_m (cm^3/mole)[a]	7.0	7.8
σ (J/cm^2)	3.7×10^{-5}	2.9×10^{-5}
D_l (cm^2/s)	10^{-5}	10^{-5}

[a]An average value of 7.4 has been taken.

fixed to $\beta^A=128.64$ cm s^{-1} K^{-1} and $\beta^B=153.60$ cm s^{-1} K^{-1}, not far from the actual best estimates [30] and a realistic value for the interface thickness was selected as 1.68×10^{-7} cm. With these values it results $W^A=0.963$; $W^B=0.960$; $m^A=m^B=350$.

III. THE NUMERICAL METHOD

The evolution of Eqs. (24)–(26) has been considered in one spatial dimension, in the domain $0\leqslant x\leqslant x_m$ with x_m large enough to prevent finite size effects. Fluxless boundary conditions for ϕ,c and transparent conditions for T were imposed at the domain's walls. To discretize the equations second order in space and first order in time finite-difference approximations were utilized; then, an explicit scheme was employed to advance the solution forward in time. To ensure an accurate resolution of both the phase field and concentration profiles, the grid spacing was selected as $\Delta x=4\times10^{-4}$, that is one-half the nominal interface thickness; a time step $\Delta t=2\times10^{-10}$ was required for numerical stability. To verify the accuracy of the numerical scheme, at each time step the solute conservation was checked and in all the simulations was verified within 0.001%. The initial temperature profile is defined as

$$T(x,0)=\overline{T_I}+G(x-x_0), \tag{33}$$

with a phase boundary at temperature $\overline{T_I}$ separating the solid region ($x<x_0,\phi=0$) and the liquid region ($x>x_0,\phi=1$). The initial solute concentration is set to the equilibrium values in the two phases. Then the temperature profile is pulled towards the positive x direction, starting the solidification process.

IV. NUMERICAL RESULTS

A. The basic steady state

At first we characterized the solidification process in steady conditions, determining the two constitutional laws $k(v)$ and $T_I(v)$ which describe the interface dynamics; the stability of this basic state will be investigated in the next subsection. Some of the results reported in the following were published elsewhere [27], and are included here for the sake of completeness.

The initial concentration of the alloy was set to $c_{-\infty}=0.056\,09$ in the solid phase and $c_{+\infty}=0.070\,68$ in the liquid phase, corresponding to an equilibrium temperature $T_I=1706.06$ K. To force stable growth we chose a high value of the temperature gradient ($G=200$ K); with this value after an initial transient solidification proceeded at constant rate and with uniform concentration $c_{+\infty}$ in the solid phase. The solute segregation on the moving front was evaluated computing the minimum and maximum values c_s^*, c_l^* of the solute concentration across the interface, and defining the partition coefficient as $k(v)=c_s^*/c_l^*$; the interface temperature was determined interpolating the temperature field at $x(\phi=0.5,t)$.

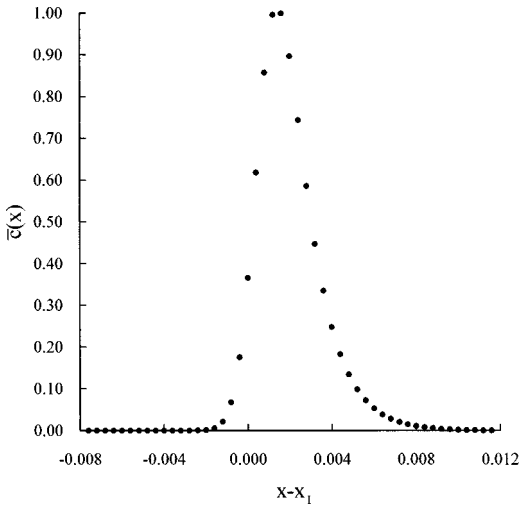

FIG. 1. Normalized concentration profile for $V_0=800$; x_I represents the position of the solid-liquid interface.

To compare our findings with the predictions of the continuous growth model (CGM) we recall that the latter gives the dependence of the partition coefficient on the growth velocity in the form

$$k(v)=\frac{k_e+v/v_d}{1+v/v_d}, \tag{34}$$

with k_e the equilibrium value for a stationary interface, and v_d a characteristic velocity describing the diffusional solute redistribution across the moving front; v_d is generally expressed as $v_d=D/a$, where D is an interface diffusivity and a is the width of the phase transition layer. In the same model the dependence of the interface temperature on velocity is given, for dilute alloys, by

$$T_I(v)=T^A+\frac{m_l c_l}{1-k_e}\{1-k+[k+(1-k)\gamma]\ln(k/k_e)\}-\frac{v}{\beta^A}, \tag{35}$$

where m_l is the slope of the equilibrium liquidus line; the parameter γ describes the dissipation of free energy due to solute drag across the interface [31]: this phenomenon is completely neglected with $\gamma=0$ and accounted for with $\gamma=1$.

Figure 1 shows the solute profile normalized as $\overline{c}(x)=[c(x)-c_{+\infty}]/(c_l^*-c_{+\infty})$, for $V_0=800$. The graph displays in an instructive way the diffuse interface nature of the present model: we observe that the transition of $\overline{c}(x)$ takes place within a length that is approximately $a=2\times10^{-3}$; with D being bounded as $D_s<D<D_l$, we expect a value of $v_d<500$. This prediction is confirmed in Fig. 2 where the partition coefficient is represented versus the growth velocity v; the solid dots refer to the results of the present simula-

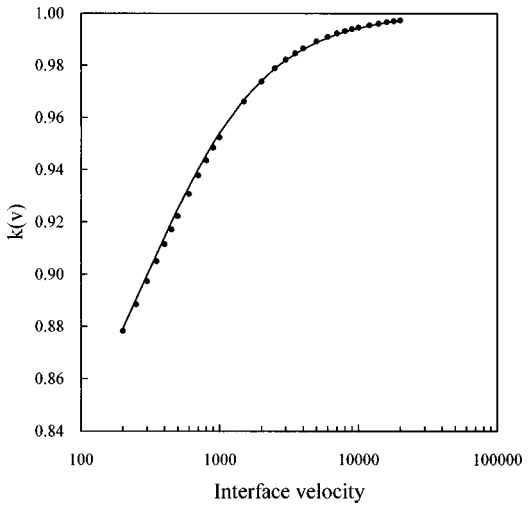

FIG. 2. Partition coefficient $k(v)$ versus the front velocity. The solid dots correspond to the values c_s^*/c_l^* of the present simulations; the solid line is drawn through Eq. (34) with $v_d = 290$ (best fit value).

tions, whereas the continuous line was drawn through Eq. (34). Using v_d as an adjustable parameter, the best fit was found at $v_d = 290$.

Figure 3 shows the numerical results for the $T_I(v)$ dependence; on the same graph we superimposed the curves computed through Eq. (35) corresponding to $\gamma = 0$ (neglecting solute drag), $\gamma = 1$ (complete solute drag), and to the best fit value $\gamma = 0.65$. Notice that the phase-field model suggests a picture of the solidification process characterized by *partial solute drag*; this feature can be related to the diffuse interface nature of the model [10,31]; it should also be observed that experimental evidence of partial solute drag has been found in an experimental study on dendritic solidification [32].

B. The oscillatory instability

The $T_I(v)$ curve shown in Fig. 3 exhibits a nonmonotonic behavior: due to suppression of solute partitioning (and to the reduction of solute concentration on the liquid side of the interface), at low velocities $T_I(v)$ first rises, then falls with increasing v reflecting the increasing undercooling required to advance the solidification front. In the range of positive slope the driving force for the process (i.e., the thermodynamic undercooling) is a decreasing function of the associated flux (the growth rate) and instabilities must be expected. Two different pictures can arise, depending on the selected isotherm velocity and the restabilizing effect of the temperature gradient. Figure 4 shows the interface velocity versus time, for $V_0 = 1200$ and $G = 40$ K. The initial condition is rapidly reabsorbed; after a few damped oscillations the system settles on its steady state with $v = V_0$. A totally different dynamic behavior emerges from Fig. 5, where the interface velocity and temperature are represented versus time, for $V_0 = 700$ and $G = 40$ K: the process never reaches a steady regime, and the interface velocity continuously oscillates around the average value V_0. These results agree with previous findings of Merchant *et al.* [33] and Brattkus and Meiron [34] which predicted relaxation oscillations of the

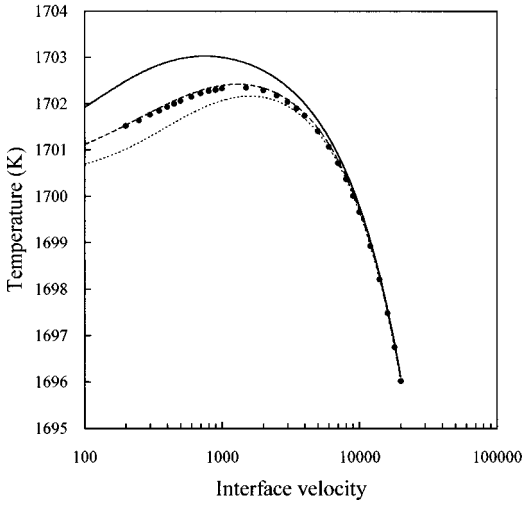

FIG. 3. Interface temperature versus interface velocity for steady growth. Solid dots: results of the present model. The predictions of the continuous growth model are given by the solid, dashed, and dotted lines for $\gamma = 0$, 0.65, and 1, respectively.

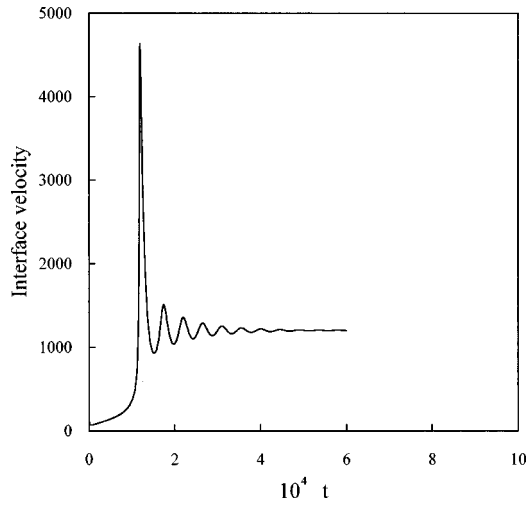

FIG. 4. The interface velocity versus time. The isotherm velocity is $V_0 = 1200$ and the temperature gradient is $G = 40$ K.

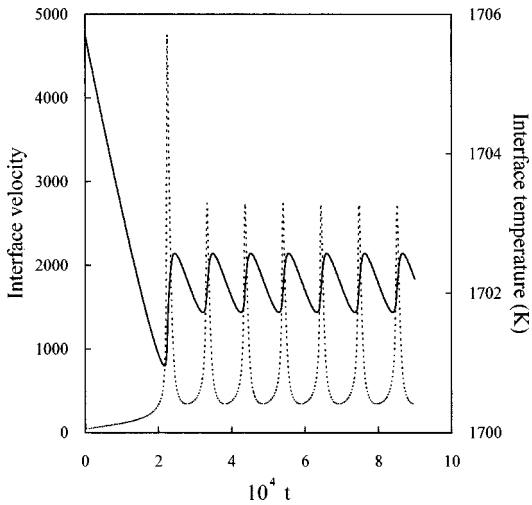

FIG. 5. Interface velocity (dotted line) and temperature (solid line) versus time. The isotherm velocity is $V_0 = 700$ and the temperature gradient is $G = 40$ K.

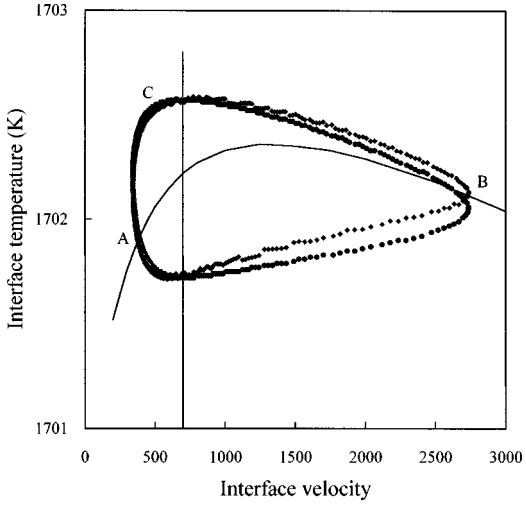

FIG. 6. The orbit followed by the process in the T_I, v plane; the isotherm velocity is indicated by the vertical line ($V_0=700$); $G=40$ K. Solid dots: results of the present simulation; diamonds: predictions of the continuous growth model assuming $c_l=c_l^*$ and $\gamma=0.65$. The solid line indicates the steady $T_I(v)$ curve. The meaning of the points A,B,C is illustrated in the text.

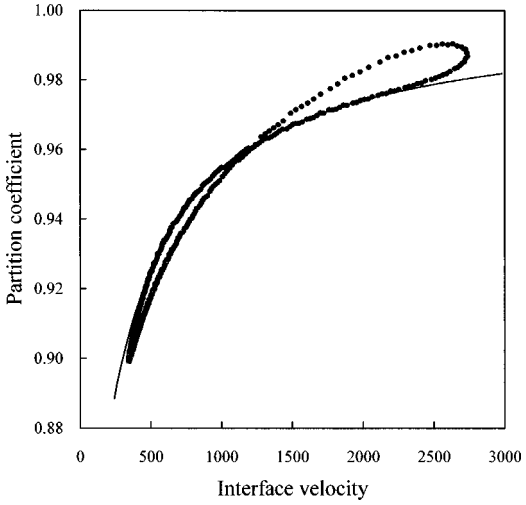

FIG. 7. Partition coefficient $k(v)$ versus the front velocity, with $V_0=700$ and $G=40$ K. The solid dots correspond to the values c_s^*/c_l^* of the present simulations; the solid line is drawn through Eq. (34) with $v_d=290$ (best fit value).

interface speed starting from the free-boundary diffusional formulation of the problem. The orbit followed by the system in the T_I,v plane is shown in Fig. 6 (solid dots). The vertical line indicates the isotherm velocity $V_0=700$; on the same graph the solid line is the steady $T_I(v)$ curve, and the diamonds represent the data calculated along the predictions of the CGM, i.e., through Eqs. (34) and (35) with $\gamma=0.65$ and using the actual values of c_l^* for the solute concentration in the liquid. For most of the cycle the interface velocity is lower than V_0 and the interface cools down; then the orbit traverses the steady $T_I(v)$ curve at point A, where the front velocity is not far from V_0 and with a strong acceleration reaches point B on the stable branch. Here the interface velocity is much higher than V_0 and the interface warms up; solidification is decelerated and the operating point shifts to C. Notice that the shape of the cycle can be modified when the latent heat diffusion is taken into account [13]. The orbit predicted by the CGM closely resembles the actual cycle performed by the solidification front; however, some differences arise which are discussed in the following. The continuous growth model, if not regarded from a proper perspective, can originate ambiguities and inconsistent results. It supplies the nonequilibrium conditions needed to solve the free-boundary diffusional problem; these conditions are applied on the moving front that is treated, under all respects, as a zero-dimension interface. But the model itself is intrinsically based on a diffuse interface picture of the solidification process, where it describes the solute reequilibration through the finite diffusional velocity v_d. This ambiguity, accurately clarified in the original papers of Aziz [9], Aziz and Kaplan [10], and Aziz and Boettinger [31], was in the past at the origin of some misunderstandings. Equations (34) and (35), derived for steady growth, are generally assumed to work even for a time dependent process; on the contrary solute relaxation across the interface is not instantaneous but takes a time of the order $\tau\sim a^2/D=a/v_d$, and conditions (34) and (35) give an unrealistic picture of the interface dynamics when the transient characteristic time is of the order of τ (or the characteristic frequency is of the order of $1/\tau$). This is precisely the situation depicted in Figs. 5 and 6: τ is here of the order of 10^5, and the fast transients shown in Fig. 5 exhibit Fourier components comparable with $1/\tau$; then conditions (34) and (35) should not be consistent with the results of the present model. This suggestion is confirmed by Fig. 7, where we have compared the cycle described by the ratio c_s^*/c_l^* (solid dots) with the partition coefficient $k(v)$ predicted by Eq. (34) (solid line). We note that c_s^*/c_l^* is not a uniquely defined function of the interface velocity, showing a hysteretic behavior and deviating from $k(v)$ during a significant portion of the cycle.

Due to the above arguments, we do not expect a sharp agreement between our results and the predictions of the linear analysis performed by Merchant and Davis [8]. Assuming a periodic perturbation parallel to the advancing front of the form $\exp(iqy+\omega t)$ they determined the region in the parameter space where the oscillatory instability should arise, i.e., where $\mathrm{Re}(\omega)>0$ and $\omega_I=\mathrm{Im}(\omega)\neq 0$; the dependence of the oscillation frequency on the relevant parameters that characterize the process was also determined. Their results (corrected to account for the partial solute drag effect) are compared to our present simulations in Fig. 8, where the oscillation frequency is represented versus the isotherm velocity, with $G=40$ K. The solid line corresponds to the predictions of the linear analysis (due to an erroneous estimation of m_l, in a previous paper [29] these data were incorrectly reported); the solid dots give the results of our simulations. The instability range is bounded between $150<V_0<1200$ for the linear analysis and between $150<V_0<1000$ for the present model. It is worth observing that, as it could have been expected, the agreement is better at low frequency.

Figure 9 shows ω_I versus the temperature gradient G, with $V_0=600$; the linear analysis predicts higher frequencies and a more extended instability range: oscillations are suppressed at $G>70$ K in the present simulations, and at $G>120$ K for the linear analysis.

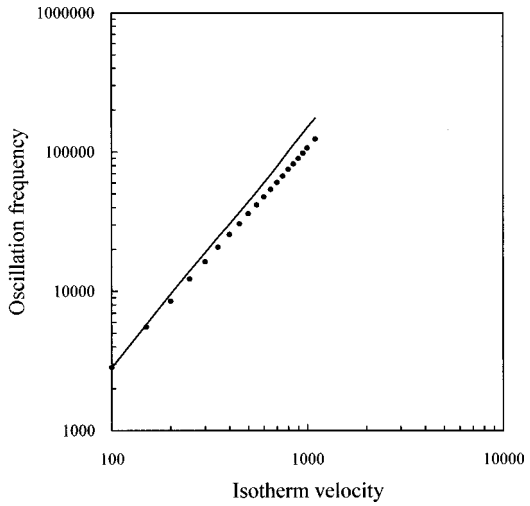

FIG. 8. The oscillation frequency versus the isotherm velocity; $G=40$ K. Solid line: as predicted by the linear stability analysis. Solid dots: solutions found in the present simulations. The instability range is bounded between $150<V_0<1200$ for the linear analysis and between $150<V_0<1000$ for the present model.

The oscillating behavior of the interface dynamics has a strong influence on the structure of the solidified alloy. In Fig. 10 we show the time dependence of c_s^* and c_l^*; on the same graph the interface velocity is also shown. Here $V_0=700$ and $G=40$ K, corresponding to $\mathrm{Re}(\omega)>0$. We observe that at low velocities c_s^* reaches its minimum; then the interface accelerates, solute partitioning is suppressed, and c_s^* increases. Notice that due to the depletion of solute ahead of the interface (see the c_l^* curve) the maximum of c_s^* anticipates the maximum of v. Then, as velocity diminishes, solute segregation becomes again effective and c_s^* decreases.

In Fig. 11 we show the concentration profile with $V_0=700$ and $G=40$. We observe low and high concentration solute bands which reflect the periodic variations of $c_s^*(t)$. The wavelength of the solute concentration profile has been

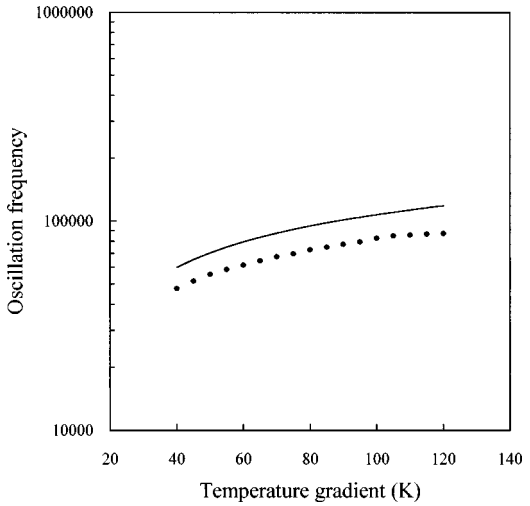

FIG. 9. The oscillation frequency versus the temperature gradient; the isotherm velocity is $V_0=600$. Solid line: as predicted by the linear stability analysis. Solid dots: solutions found in the present simulations. The instability range extends up to $G=70$ K in the present simulations, and to $G=120$ K for the linear analysis.

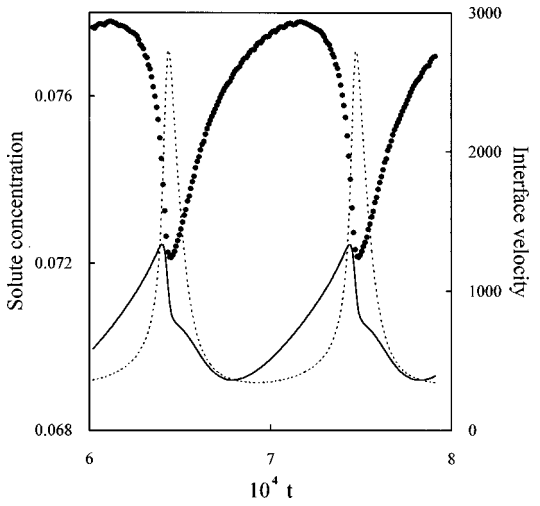

FIG. 10. Time variation of c_l^* (solid dots), c_s^* (solid line), and the interface velocity (dotted line). The isotherm velocity is $V_0=700$ and the temperature gradient is $G=40$ K.

estimated as $\lambda=0.0724$, which is practically coincident with the expected value $2\pi V_0/\omega_I=0.0727$.

V. CONCLUSIONS

In summary, we addressed rapid directional solidification through the phase-field model, which provides an efficient way to treat nonequilibrium effects as solute trapping and kinetic undercooling of the solid-liquid interface. In steady conditions we recovered with good agreement the results of the free-boundary equations, with interface conditions given by the continuous growth model; the dissipation of free energy at the growing front seems to be properly described assuming partial solute drag. In a region of the parameter space the interface dynamics enters an oscillatory regime characterized by periodic variations of the growth rate. Here, due to the fast transients involved, the interface conditions provided by the CGM no longer work, and the results of the phase-field simulations deviate, to some extent, from the predictions of the free-boundary model.

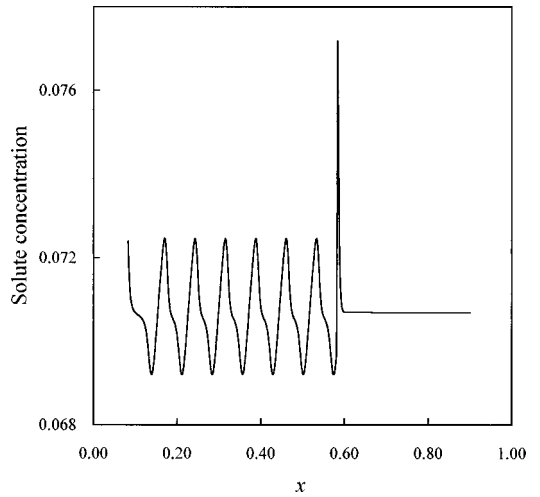

FIG. 11. Solute concentration profile along the growth direction. The isotherm velocity is $V_0=700$, and the temperature gradient is $G=40$ K.

Due to numerical tractability, in this study we neglected the latent heat released at the solid-liquid interface, assuming an infinite thermal diffusivity. As shown by Karma and Sarkissian [13], relaxing this approximation leads to an increase of the effective temperature gradient probed by the advancing front, and to a reduction of the parameter range where the oscillatory instability should be expected; nonetheless, the basic mechanism underlying the formation of solute bands should have been properly evidenced. In view of future extensions and refinements in this subject, it is worth noting that the phase-field model allows an easy description of rapid solidification processes even for concentrated solutions, with no limitations due to the actual shape of the alloy phase diagram, while at present the free-boundary approach can only be applied to very dilute solutions, when the alloy phase diagram can be conveniently linearized.

[1] M. Zimmermann, M. Carrard, and W. Kurz, Acta Metall. **37**, 3305 (1989).
[2] M. Zimmermann, M. Carrard, M. Gremaud, and W. Kurz, Mater. Sci. Eng., A **134**, 1278 (1991).
[3] M. Gremaud, M. Carrard, and W. Kurz, Acta Metall. Mater. **38**, 2587 (1990).
[4] W. J. Boettinger, D. Shechtman, R. J. Schaefer, and F. S. Biancaniello, Metall. Trans. A **15**, 55 (1984).
[5] M. Carrard, M. Gremaud, M. Zimmermann, and W. Kurz, Acta Metall. Mater. **40**, 983 (1992).
[6] W. W. Mullins and R. F. Sekerka, J. Appl. Phys. **35**, 444 (1964).
[7] S. R. Coriell and R. F. Sekerka, J. Cryst. Growth **61**, 499 (1983).
[8] G. J. Merchant and S. H. Davis, Acta Metall. Mater. **38**, 2683 (1990).
[9] M. J. Aziz, J. Appl. Phys. **53**, 1158 (1982).
[10] M. J. Aziz and T. Kaplan, Acta Metall. **36**, 2335 (1988).
[11] D. A. Huntley and S. H. Davis, Acta Metall. Mater. **41**, 2025 (1993).
[12] A. Karma and A. Sarkissian, Phys. Rev. Lett. **27**, 2616 (1992).
[13] A. Karma and A. Sarkissian, Phys. Rev. E **47**, 513 (1993).
[14] G. Caginalp, in *Applications of Field Theory to Statistical Mechanics*, edited by L. Garrido, Lecture Notes in Physics Vol. 216 (Springer, Berlin, 1984), p. 216.
[15] G. Caginalp, Arch. Ration. Mech. Anal. **92**, 205 (1986).
[16] G. Caginalp and P. Fife, Phys. Rev. B **33**, 7792 (1986).
[17] O. Penrose and P. C. Fife, Physica D **43**, 44 (1990).
[18] S. L. Wang, R. F. Sekerka, A. A. Wheeler, B. T. Murray, S. R. Coriell, R. J. Braun, and G. B. McFadden, Physica D **69**, 189 (1993).
[19] A. A. Wheeler, B. T. Murray, and R. J. Schaefer, Physica D **66**, 243 (1993).
[20] H. Lowen, J. Bechhofer, and L. Tuckerman, Phys. Rev. A **45**, 2399 (1992).
[21] F. Marinozzi, M. Conti, and U. Marini Bettolo Marconi, Phys. Rev. E **53**, 5039 (1996).
[22] A. A. Wheeler, W. J. Boettinger, and G. B. McFadden, Phys. Rev. A **45**, 7424 (1992).
[23] A. A. Wheeler, W. J. Boettinger, and G. B. McFadden, Phys. Rev. E **47**, 1893 (1993).
[24] G. Caginalp and W. Xie, Phys. Rev. E **48**, 1897 (1993).
[25] M. Conti, Phys. Rev. E **55**, 701 (1997).
[26] M. Conti, Phys. Rev. E **55**, 765 (1997).
[27] M. Conti, Phys. Rev. E **56**, 3717 (1997).
[28] J. A. Warren and W. J. Boettinger, Acta Metall. Mater. **43**, 689 (1995).
[29] M. Conti, Phys. Rev. E **56**, R6267 (1997).
[30] R. Willnecker, D. M. Herlach, and B. Feuerbacher, Phys. Rev. Lett. **62**, 2707 (1989).
[31] M. J. Aziz and W. J. Boettinger, Acta Metall. Mater. **42**, 527 (1994).
[32] K. Eckler, D. M. Herlach, and M. J. Aziz, Acta Metall. Mater. **42**, 975 (1994).
[33] G. J. Merchant, R. J. Braun, K. Brattkus, and S. H. Davis, SIAM (Soc. Ind. Appl. Math.) J. Appl. Math. **52**, 1279 (1992).
[34] K. Brattkus and D. I. Meiron, SIAM (Soc. Ind. Appl. Math.) J. Appl. Math. **52**, 1303 (1992).